Check for updates

Solar thermochemical CO_2 splitting with doped perovskite $LaCo_{0.7}Zr_{0.3}O_3$: thermodynamic performance and solar-to-fuel efficiency

Lei Wang, [iD] [ab] Tianzeng Ma, [ab] Shaomeng Dai, [ab] Ting Ren, [a] Zheshao Chang, [a] Mingkai Fu, [iD] *[a] Xin Li [ab] and Yong Li [iD] *[c]

The research of thermochemical CO_2 splitting based on perovskites is a promising approach to green energy development. Performance evaluation was performed towards the doped perovskite $LaCo_{0.7}Zr_{0.3}O_3$ (LCZ-73) based two-step thermochemical CO_2 splitting process thermodynamically based on the experimentally derived parameters for the first time. The impacts of vacuum pump and inert gas purge to reduce oxygen partial pressure and CO_2 heating on the performance parameter $\eta_{solar\text{-}to\text{-}fuel}$ have been analyzed. The results showed that at the P_{O_2} of 10^{-5} bar, non-stoichiometric oxygen δ increased by more than 3 times as the reduction temperature varied from 1000 °C to 1300 °C, however, no significant deviation of δ was observed between 1300 °C and 1400 °C. The reaction enthalpy ranged from 60 to 130 kJ mol^{-1} corresponding to $\delta = 0.05–0.40$. Comparing the abovementioned two ways to reduce the oxygen partial pressure, the $\eta_{solar\text{-}to\text{-}fuel}$ of 0.39% and 0.1% can be achieved with 75% and without heat recovery with the CO_2 flow rate of 40 sccm under experimental conditions, respectively. The energy cost for CO_2 heating during the thermodynamic process as the $n_{CO_2}/n_{LCZ\text{-}73}$ increases was obtained from the perspective of energy analysis. The ratio of $n_{CO_2}/n_{LCZ\text{-}73}$ at lower temperature required more demanding conditions for the aim of commercialization. Finally, the ability of perovskite to split CO_2 and thermochemical performance were tested under different CO_2 flow rates. The results showed that high CO_2 flow rate was conducive to the production of CO, but at the cost of low $\eta_{solar\text{-}to\text{-}fuel}$. The maximum solar-to-fuel efficiency of 1.36% was achieved experimentally at a CO_2 flow rate of 10 sccm in the oxidation step and 75% heat recovery.

1. Introduction

CO_2 is the main greenhouse gas of the Earth because of its stable thermodynamic properties and large amounts of emission in a short period of time.[1] Thermochemical CO_2 splitting is an effective method to mitigate CO_2 emissions and provide a sustainable energy development path.[2] As the most abundant energy source on the Earth, solar energy is clean and pollution-free, and has received the attention of many countries in the world. Using solar energy as a source of energy for thermochemical fuel production can effectively alleviate the global energy crisis and global warming effect.[3,4] Solar thermochemical CO_2 splitting takes sufficient solar energy as the heat source and greenhouse gas CO_2 as the carbon source, which can realize the sustainable production of carbonaceous fuel,[5,6] and can be converted into liquid fuels through existing industrial facilities

for long-distance transportation and storage.[7] At the same time, in this process, discontinuous and low energy density solar energy is stored in the form of fuel chemical energy with high energy density.

The solar two-step thermochemical fuel production with metal oxide perovskite, ABO_3, as the oxygen carrier has received more and more attention from the researchers in recent years.[8,9] Compared to the more studied binary oxide cerium oxide, perovskites have the advantage of being able to be reduced at lower operating temperatures, while having a greater amount of oxygen released so that more fuel can be produced in the oxidation step.[10,11] In recent years, it has been reported that perovskite is used as oxygen carrier to split CO_2 for CO production.[12,13] Dey *et al.* studied the substituted $La_{0.5}Sr_{0.5}MnO_3$ with trivalent metal ion at B site, and the results showed that the performance of thermochemical CO_2 splitting was significantly improved by 5% Sc substitution at B position, and the yield of O_2 and CO increased by 2 times and 1.7 times, respectively.[14] Muhich *et al.* compared the performance of perovskite and ceria in thermochemical splitting of CO_2, and found that perovskite has a high CO production capacity under a large CO_2 flow rate, but at the same time, the solar-to-fuel efficiency is lower due to

[a]Institute of Electrical Engineering, Chinese Academy of Sciences, Beijing, 100190, China. E-mail: fumingkai@mail.iee.ac.cn

[b]University of Chinese Academy of Sciences, Beijing, 100190, China

[c]School of Mechanical Engineering, University of Science and Technology Beijing, Beijing 100083, China. E-mail: liyong@ustb.edu.cn

the high heating cost.[15] Ezbiri *et al.* extensively screened the perovskite redox activity and thermochemical stability used for solar thermochemical splitting of CO_2 by density functional theory, and verified the calculation results through experiments and applied them to fine-tune the oxygen exchange capacity of selected perovskite components.[16] Galvez and coworkers studied the splitting of CO_2 by Ca and Sr-doped $LaMnO_3$ perovskites and found that the formation of carbonates resulted in a decrease in thermochemical efficiency due to incomplete conversion of CO_2.[17] Demont *et al.* studied the solar CO_2 splitting *via* two-step thermochemical cycle with A- and B-site substituted Mn-perovskites, the results showed the effectiveness of the incorporation of Y in A-site and Mg in B-site in terms of CO production when compared with ceria.[18] Cooper *et al.* studied $LaMnO_3$ perovskite with Ca/Sr A-site and Al B-site doping for CO_2 splitting, the results show that these materials could split CO_2 into CO at 1240 °C and could approach complete oxidation at 1040 °C. The fuel production per unit mass was 10 times that of CeO_2 under the same conditions.[19] Bork and coworkers found a material, $La_{0.6}Sr_{0.4}Cr_{0.8}Co_{0.2}O_{3-\delta}$ with efficient solar-to-fuel conversion at lower temperatures. Thermogravimetric experiments showed that the ability to decompose CO_2 is more than 25 times that of CeO_2 in the two-step thermochemical cycle of 800–1200 °C.[20] Demont *et al.* studied the splitting of CO_2 by two-step solar thermochemical of $LaMnO_3$ perovskite doped with Sr, and characterized the redox thermodynamics properties. The results showed that a certain amount of Sr can tune the redox thermodynamics of the series of materials, which has a high activity for the splitting of CO_2.[21] Takalkar *et al.* studied the thermochemical CO_2 splitting by $Pr_xSr_{1-x}MnO_3$ perovskites by thermogravimetry. It was found that lower Pr and higher Sr can effectively increase CO production, and two optimal perovskites were identified as promising materials for thermochemical CO_2 splitting.[22] Jiang *et al.* studied the loaded $LaFeO_3$ perovskite with A- and B-sites doping. The CO production increased by 2–3 times, and the controlling mechanism and kinetic model of CO_2 splitting process were analyzed.[23]

Currently, in the two-step thermochemical CO_2 splitting with perovskite as the oxygen carrier, most of the researches focus on one or the perovskite series through the different contents of elemental doping. The main goal of the studies is to find a high-performance perovskite that increases fuel production and thus achieves high solar-to-fuel efficiency ($\eta_{solar-to-fuel}$). The direction of efforts is mainly focused on the improvement of redox thermodynamics, kinetic properties and thermal stability of the material thermochemical cycle. Although researchers have made a lot of efforts in these areas and made great progress in some areas, the current researches in the field of thermochemical fuel research have low efficiency and cannot be commercialized. At present, the world's largest thermochemical fuel system is in pilot scale,[24] and how to achieve efficient fuel production remains a major challenge. It is beneficial to explore materials that can balance the advantages of reduction and oxidation reactions, and thermodynamic analysis should be performed when conducting primary materials screening.[25] However, there are few studies on the thermodynamics of

perovskite thermochemical fuel production. Thermodynamic analysis was only performed theoretically in literatures. Carrillo and Scheffe established a thermodynamic model to calculate the solar-to-fuel efficiency of $La_{1-x}(Sr,Ca)_xMn_{1-y}Al_yO_3$ perovskites, showing the potential to improve the efficiency during isothermal or near-isothermal thermochemical cycles.[26] Muhich *et al.* implemented a thermodynamic system model of solar thermochemical fuel production based on mass and energy balances, the results showed the promising of perovskites due to the high fuel production capacities under large H_2O/CO_2 flow rates, but the poor solar-to-fuel efficiency due to the high heating load.[15] Bork *et al.* performed a Calphad defect model to optimize and calculate the redox thermodynamics of Cr-doped $La_{0.6}Sr_{0.4}MnO_3$ perovskite for solar-to-fuel conversion, the results revealed that both the thermochemical fuel production and the solar-to-fuel efficiency of the Cr-doped materials were improved. These predictive perspectives are expected to provide prospects for the thermodynamic engineering of perovskite thermochemical reactions towards high solar-to-fuel efficiency.[27] Overall, the existing studies on thermodynamic analysis and solar-to-fuel efficiency mainly focus on theoretical analysis, but the extent to which level of this efficiency, especially the solar-to-fuel efficiency still needs more experimental proof.

To our knowledge, there are no studies addressing the thermodynamic analysis of CO_2 conversion into fuels using Zr doped $LaCoO_3$. This paper focuses on the report of a detailed thermodynamic analysis of a two-step thermochemical CO_2 splitting process with perovskite $LaCo_{0.7}Zr_{0.3}O_3$ (LCZ-73) as the oxygen carrier based on the obtained thermodynamic parameters experimentally. Material synthesis, characterization and thermochemical performance of CO_2 splitting have been reported in the previous experimental work,[28] in which studies of elements doping, doping concentration, the redox temperatures, heating rates on the performance of the doped $LaCoO_3$ perovskites based two-step thermochemical CO_2 splitting and reduction kinetics were illustrated. The results demonstrated the stability of the material before and after the thermochemical redox cycles, the activity of thermochemical CO_2 splitting and better reduction kinetics than other perovskite metal oxides and cerium oxides reported in the literature. These studies focused on discussing the performance of thermochemical CO_2 splitting from the perspective of experiments, but did not involve the thermodynamics of this process. Therefore, this paper discussed the thermodynamics of thermochemical CO_2 splitting from the perspective of solar to fuel conversion. The thermochemical reduction enthalpy was obtained and the thermodynamic efficiency was analyzed with the consideration of gas–gas, gas–solid phase heat recuperation as well as the use of vacuum pump and vacuum pump combined with inert gas purge to reduce the oxygen partial pressure. Based on the experimental conditions, the solar-to-fuel efficiency of the solar thermochemical fuel production process was analyzed by combining the vacuum pump with the inert gas purge and directly the vacuum pump to reduce the oxygen partial pressure, respectively. The energy consumed for CO_2 heating took up the bulk of energy consumption of the thermodynamic process as the n_{CO_2}/n_{LCZ-73}

increases based on the energy analysis. Finally, the thermodynamic model was verified by experimentally testing the CO_2 splitting performance under different CO_2 flow rates and analyzing its solar-to-fuel efficiency. This paper revealed that one of the main problems in the field of solar thermochemical fuel production was the huge energy input caused by excessive oxidant in the oxidation step, which resulted in low efficiency.

2. Experiment and mathematical model

2.1. Experimental procedure and apparatus

$LaCo_{0.7}Zr_{0.3}O_3$ perovskite powder was prepared by citric acid sol–gel method, which was described in detail in previous studies.[28] Metal nitrate precursors were obtained commercially (Aladdin and Macklin) and were specified to be >99.5% pure. XRD measurements confirmed the existence of perovskite structure $LaCo_{0.7}Zr_{0.3}O_3$, SEM image showed that the sample was irregularly shaped particles with a size in the a few microns and EDS analysis verified that the synthesized sample compositions were in line with expectations. Similarly, XRD of the powder sample after reduction showed that it still maintained the perovskite phase structure. The measurements of the redox reactions were carried out with a high temperature thermogravimetric analyzer (TGA, LINSEIS STA PT 1600). To avoid the effects of thermal inertia during testing, fresh material of $LaCo_{0.7}Zr_{0.3}O_3$ (LCZ-73) oxide of the same batch of synthetic sample powder was used in each test. Granular powders with an average weight of approximately 10 mg were evenly placed in an alumina crucible with a volume of about 100 μl throughout all the measurement series. Before the formal start of the redox experiments, a vacuum pump was used to vacuum the furnace chamber to 5.5×10^{-5} atm for a low oxygen environment, and then purged with high purity argon (99.999%) for one hour to provide an inert environment and further reduce the oxygen partial pressure. The inert atmosphere was always maintained throughout the reduction process and during the process of reducing from reduction temperature to the oxidation temperature to blow the released oxygen out of the furnace in time. High purity argon was used as

the purge and protective gas, the same high purity carbon dioxide (99.999%) was used as the oxidant during the oxidation process. The overall gas flow rate entering the reaction chamber was maintained at 80 sccm, with the balance being protected with argon flow of 40 sccm at all times. In the reduction process, the sample was heated to 1000, 1100, 1200, 1300, 1400 °C, respectively, at a heating rate of 30 °C min⁻¹ and maintained for 60 min with continuous and constant Ar flow. Then the temperature was lowered to 800 °C at the same rate for oxidation. In the oxidation step, the high purity Ar (40 sccm) and high purity CO_2 with a flow rate of 40 sccm ($P_{CO_2} = 0.5$ atm) were mixed and introduced into the furnace chamber to react with the oxygen-deficient perovskite and produce CO. The trace oxygen was blown out and diluted to further reduce the impact on CO_2 splitting. This oxidation process proceeded for 60 min. The specific experimental platform was shown in the Fig. 1.

Since the redox behavior analysis of perovskite in this work was mainly based on thermogravimetric analysis, the mass change in sample was induced by the release and uptake of oxygen under high temperatures and specific oxygen partial conditions, then the non-stoichiometry of the perovskite can be determined by measuring the mass change. The relationship between the mass change Δm and the nonstoichiometric oxygen δ is as follow:[29]

$$\delta = \frac{\Delta m}{\overline{M}_O} \times \frac{\overline{M}_{perovskite}}{m_{perovskite}} \qquad (1)$$

$m_{perovskite}$ is the initial mass of the perovskite sample, and $\overline{M}_{perovskite}$ and $\overline{M}_O$ are the molar mass of the perovskite and the atomic oxygen, respectively.

Thermodynamic parameters are extracted from the Van't Hoff approach. The standard molar Gibbs free energy of the reduction reaction can be expressed as follow:[8,30]

$$\Delta G^\Theta(T) = -\bar{R}T \ln K_{red} = \Delta H^\Theta_{red} - T\Delta S^\Theta_{red} \qquad (2)$$

where K_{red} is the equilibrium constant, and $K_{red} = P_{O_2}/P^\Theta$. P_{O_2}, P^Θ, $\bar{R}$ and T are the oxygen partial pressure, the standard pressure and $P^\Theta = 1$ bar, the universal gas constant and the
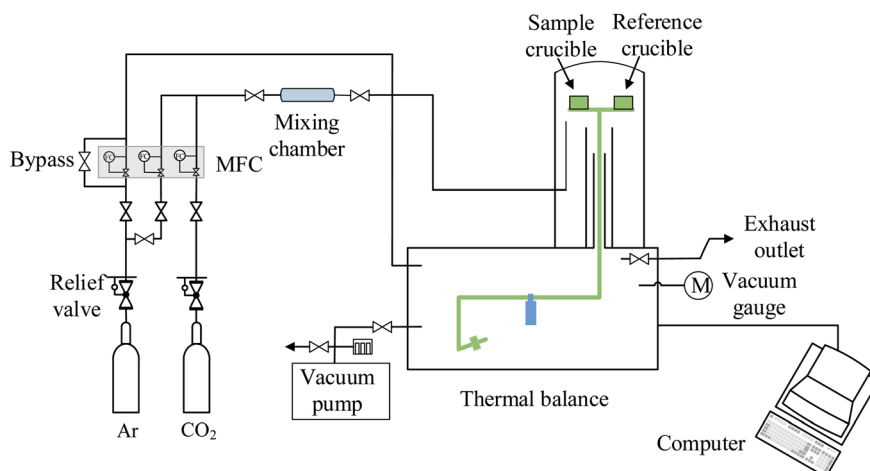

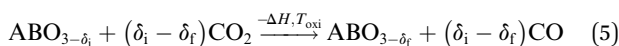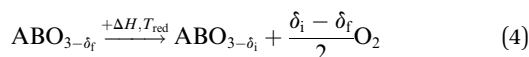**Fig. 1** Schematic diagram of the experimental platform for thermochemical CO_2 splitting.

reduction temperature, respectively. Inserting the relationship of K_{red} into eqn (1), for constant oxygen non-stoichiometry, δ, the above equation can be rearranged as

$$\ln\left(\frac{P_{O_2}}{P^\Theta}\right)\Bigg|_{\Delta\delta=constant} = -\frac{\Delta H_{red}^\Theta}{\bar{R}T} + \frac{\Delta S_{red}^\Theta}{\bar{R}} \qquad (3)$$

$\Delta\bar{H}_{red}^\Theta$ is the standard molar enthalpy and can be determined through an Arrhenius plot for sets of temperature T and $\ln(P_{O_2})$.

2.2. Mathematical model

A typical thermochemical redox cycle of CO_2 splitting for a two-step process based on perovskite can be exemplified in the following reactions:

$$ABO_{3-\delta_f} \xrightarrow{+\Delta H, T_{red}} ABO_{3-\delta_i} + \frac{\delta_i - \delta_f}{2}O_2 \qquad (4)$$

$$ABO_{3-\delta_i} + (\delta_i - \delta_f)CO_2 \xrightarrow{-\Delta H, T_{oxi}} ABO_{3-\delta_f} + (\delta_i - \delta_f)CO \qquad (5)$$

where δ_i and δ_f are the oxygen non-stoichiometry of perovskite after reduction and oxidation reactions, respectively. $\Delta\delta = \delta_i - \delta_f$ is the non-stoichiometry net change in oxygen, which is also a numerical equivalent of the amount of CO produced by 1 molar of perovskite in a single thermochemical cycle. In the first step, the perovskite oxide is partly reduced at a high reduction temperature (T_{red}), releasing lattice oxygen and generating oxygen vacancies, eqn (4). In the second oxidation step, the reduced perovskite is reoxidized by CO_2 at a lower temperature (T_{oxi}), eqn (5), CO_2 is reduced to CO. For a non-isothermal thermochemical cycle, $T_{red} > T_{oxi}$.

2.2.1. Reduction process. Here we consider a dynamic thermochemical cycle rather than a process of heating the perovskite from room temperature to reduction temperature, and a quasi-steady state is assumed for the thermochemical cycle. Thus, the energy required to heat the perovskite from oxidation temperature to reduction temperature is:

$$Q_{LCZ-73} = \int_{T_{oxi}}^{T_{red}} \bar{C}_{p,LCZ-73} dT \qquad (6)$$

The energy required to drive the reduction reaction of one molar perovskite is:

$$Q_{red} = \int_{\delta_f}^{\delta_i} \Delta H_{red}^\Theta(\delta) d\delta \qquad (7)$$

where $\bar{C}_{p,LCZ-73}$ is the molar specific heat capacity of perovskite LCZ-73 used in the test, which can be obtained by differential scanning calorimeter. According to the thermal effect obtained by differential scanning calorimetry and the formula $\Delta Q = (m/\bar{M})\bar{C}_p\Delta T$, the value of $\bar{C}_p$ can be obtained. In fact, the specific heat capacity is a function of temperature, but for convenience, the average value of $\bar{C}_{p,LCZ-73} = 157.5$ J (mol^{-1} K^{-1}) is considered.

Researches have shown that decreasing oxygen partial pressure in the thermal reduction process is beneficial to the increase of δ and the efficiency of thermochemical fuel production.[31] There are two common ways to reduce oxygen

partial pressure of the reduction process in thermochemical fuel research: vacuum pump and inert gas purge.

2.2.1.1. Pumping. A vacuum pump is needed to eliminate the residual air in the reactor to provide a lower oxygen partial pressure environment during the thermal reduction process. Q_{pump} is the energy consumed to obtain a lower oxygen partial pressure with a vacuum pump. In this paper, the ideal pump work is used to calculate the performance of solar-to-fuel efficiency.[32]

$$Q_{pump} = n_{O_2}\bar{R}T_{pump}\ln(P_0/P_{O_2})/\eta_{S\to W} \qquad (8)$$

where $n_{O_2} = n_{CO}/2$ follows from the reaction stoichiometry, $\bar{R}$ is the universal gas constant, T_{pump} is the operating temperature of the pump. In this study, the temperature is the ambient temperature. P_0 is the experimental pressure at atmospheric pressure. P_{O_2} is the oxygen partial pressure inside the instrument after vacuuming, $\eta_{S\to W}$ is the solar energy to pump work conversion efficiency and its value is assumed to be 0.1 in this paper.[32]

2.2.1.2. Sweep gas. Argon was used as the sweep gas in the reduction step and as the shielding gas for the balance chamber throughout the thermochemical process. In our experiment, high purity Ar (99.999%) with an oxygen impurity concentration less than 10 ppm was used. Considering that the high-temperature exhaust gas in the reduction process carries a large amount of heat, it can be used to preheat Ar required for the reduction reaction. Therefore, the energy required to heat sweep gas by considering the heat recovery of exhaust gas is calculated as:

$$Q_{Ar\ heating} = \left(1 - \varepsilon_{heat\ exchanger}\right)\left(n_{Ar}\int_{T_{amb}}^{T_{red}} \bar{C}_{p,Ar}(T)dT\right) \qquad (9)$$

where $\varepsilon_{heat\ exchanger}$ is the heat exchange coefficient of the heat exchanger.[33] T_{amb} is the ambient temperature and T_{red} is the reduction temperature. The molar specific heat capacity of Ar is considered constant at a certain temperature ($T \leq 2000$ K), and $\bar{C}_{p,Ar} = 20.786$ J (mol^{-1} K^{-1}).[34]

2.2.2. Oxidation process. Energy cost during the oxidation process is the cost of heating CO_2. A heat exchanger can be used to heat CO_2 using the outflowing oxidizer and fuel from the oxidation reactor. The same heat exchanger coefficient is used for simplicity.

$$Q_{CO_2\ heating} = \frac{1}{n_{LCZ-73}}\left(1 - \varepsilon_{heat\ exchanger}\right)n_{CO_2}\int_{T_{amb}}^{T_{oxi}} \bar{C}_{p,CO_2}(T)dT \qquad (10)$$

$$\bar{C}_{p,CO_2}(T) = 20.99 + 6.768 \times 10^{-2}T - 4.960 \times 10^{-5}T^2 + 1.779 \times 10^{-8}T^3 - 2.495 \times 10^{-12}T^4 \qquad (11)$$

where n_{CO_2} is the molars of CO_2 introduced in the oxidation process, T_{oxi} is the oxidation temperature, $\bar{C}_{p,CO_2}$ is the molar specific heat capacity of CO_2 under a standard atmospheric pressure and is a function of temperature T, which can be given as a polynomial fits in J (mol^{-1} K^{-1}).[33]

2.2.2.1. Heat recovery. It is difficult to realize the heat utilization of solid reactants by heating low temperature solid with high temperature solid[35] and may present some other problems. In many previous studies, the heat recovery of solid reactants was not considered.[33] The idea of using a heat exchanger to convert solid heat into process heat to heat the oxidant to improve efficiency[33] is also used in the analysis herein.

Under the experimental conditions, in order to maintain the oxidation reaction at a constant temperature, continuous additional heating is necessary. The heat transfer for one molar LCZ-73 during the oxidation reaction is calculated:

$$Q_{oxi} = -Q_{red} + (\delta_i - \delta_f)HHV_{CO} \tag{12}$$

The available amount of the recovered heat from the solid reactants is limited by the heat required for CO_2 heating in the oxidation process,

$$Q_{rec} = \begin{cases} \varepsilon_{rec}Q_{LCZ\text{-}73}, & Q_{CO_2 \text{ heating}} > \varepsilon_{rec}Q_{LCZ\text{-}73} \\ Q_{CO_2 \text{ heating}}, & Q_{CO_2 \text{ heating}} < \varepsilon_{rec}Q_{LCZ\text{-}73} \end{cases} \tag{13}$$

where ε_{rec} is the effectiveness of heat recovery. This assumes that $\varepsilon_{rec} = 0.6$ (ref. 33) and HHV_{CO} is the high calorific value of CO.

2.2.3. Solar-to-fuel efficiency. An ideal blackbody reactor is considered in the thermochemical cycling reactions, therefore, the absorption efficiency of the reactor which is a function of T_{red} and concentration ratio C.[36,37] Considering the radiative heat loss of the solar reactor, the heat required to power all the processes of the thermodynamic system can be supplied with the absorption efficiency η_{abs}. It can be defined as

$$\eta_{abs} = 1 - \frac{\sigma \times T_{red}^4}{I \times C} \tag{14}$$

Here σ is the Stefan–Boltzmann constant, 5.67×10^{-8} W $(m^{-2} K^{-4})$. $I = 1000$ W m^{-2}, C represents the solar concentration ratio in suns, here, $C = 3000$ (ref. 38 and 39) is employed in this paper. Here, we assume that there is no heat loss of convection and heat conduction from the solar reactor, thus there is only the heat loss rooted in radiation to the ambient.

An energy balance equation for the entire thermochemical processes yields the following equation:[33,38]

$$Q_{solar}$$
$$= \frac{Q_{red} + Q_{LCZ\text{-}73} + Q_{Ar \text{ heating}} + Q_{pump} + Q_{CO_2 \text{ heating}} + Q_{oxi} - Q_{rec}}{\eta_{abs}} \tag{15}$$

Here we assume that the required electrical heating energy, pumping power, energy for gas purging, CO_2 heating and energy required to maintain a constant temperature for oxidation and other energy-consuming processes of the thermochemical cycle are all provided by solar energy. The available heat recovery of the system is also considered.

According to the first law of thermodynamic, $\eta_{solar\text{-}to\text{-}fuel}$ of the two-step thermochemical redox processes is chosen as the merit of the thermochemical cycling performance,[40,41] which is defined as the ratio of the calorific value of the fuel to the total solar energy input in the system:[33,38,42]

$$\eta_{solar\text{-}to\text{-}fuel}$$
$$= \frac{\eta_{abs}(\delta_i - \delta_f)HHV_{CO}}{Q_{red} + Q_{LCZ\text{-}73} + Q_{Ar \text{ heating}} + Q_{pump} + Q_{CO_2 \text{ heating}} + Q_{oxi} - Q_{rec}} \tag{16}$$

where HHV_{CO} is the higher heating value of CO.

3. Results and discussion

3.1. Thermodynamic characteristics of LCZ-73

Here, the relationship between oxygen partial pressure and non-stoichiometric oxygen δ during the reduction process after reaching the target temperatures is revealed. As shown in Fig. 2, the non-stoichiometric oxygen δ in $LaCo_{0.7}Zr_{0.3}O_{3-\delta}$ is highly dependent on reduction temperature and the oxygen partial pressure (P_{O_2}). As the oxygen partial pressure (P_{O_2}) decreases, the non-stoichiometric oxygen δ gradually increases, but the increase rate slows down as the reduction reaction proceeds. Under the same oxygen partial pressure environment, the high temperature is more favorable for the generation of non-stoichiometric oxygen in the reduction process. But it is not that the higher the temperature is, the better it will be. At 1300 °C and 1400 °C, the ability to produce non-stoichiometric oxygen under both conditions is nearly the same. At the oxygen partial pressure of 10^{-5} bar, the non-stoichiometric oxygen at the reduction temperature of 1000–1400 °C is 0.18, 0.34, 0.44, 0.60 and 0.60, respectively. The non-stoichiometric oxygen δ increases by more than 3 times when the temperature varies from 1000 °C to 1300 °C. At 1000 °C, the non-stoichiometric oxygen δ is doubled when P_{O_2} changes from 10^{-4} to 10^{-5} bar, while, at 1300 °C, this value increases by a third. Lower oxygen partial pressure is required when the same non-stoichiometric oxygen is reached at low temperature. At $\delta = 0.2$, the oxygen partial pressure P_{O_2} during 1000–1400 °C varies from $10^{-5.75}$ to $10^{-3.55}$ bar.

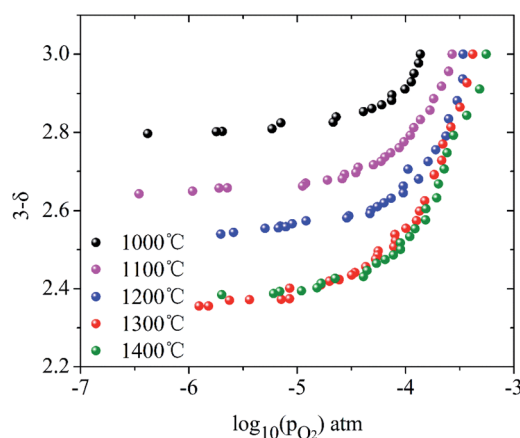**Fig. 2** Oxygen non-stoichiometry δ of ~10 mg LCZ-73 perovskite powder reduced at 1000–1400 °C for 60 min with a heating rate of 30 °C min^{-1} (in this analysis, only the reduction under a constant temperature process is considered).

Based on the above analysis, the derived $\ln(P_{O_2})$ *versus* inverse temperature for LCZ-73 is shown in Fig. 3. Considering that there is a certain error in the oxygen partial pressure at some points, the linearity is not ideal for all when performing linear fitting on the data points, especially for the $\delta = 0.20$ and $\delta = 0.25$. Similarly, it can be found that the non-stoichiometric oxygen increases with decreasing the oxygen partial pressure at the same temperature. In order to achieve the same δ, a lower oxygen partial pressure is required at low temperature. Fig. 3 also shows two ways to obtain larger non-stoichiometric oxygen δ: increasing temperature and decreasing oxygen partial pressure. According to the existing data with better linearity, it can be seen that $\Delta H_{red}^{\ominus}$ in eqn (3) is likely to be temperature-independent, which is confirmed in other studies.[30] Simultaneously, this also shows the reliability of our experimental data. Based on this, we can get the relationship between the reduction enthalpy $\Delta H_{red}^{\ominus}$ and the different oxygen stoichiometry δ during the thermochemical reduction process, which will be discussed next.

The energy required to generate oxygen vacancies in the perovskite LCZ-73 can be obtained *via* the change of reduction enthalpy, $\Delta H_{red}^{\ominus}$. Similar studies have shown that reduction enthalpy is only related to stoichiometry δ.[8,43] As shown in Fig. 4, the curve for the change in standard molar reduction enthalpy is fit with a polynomial. The value of $\Delta H_{red}^{\ominus}$ is 60–130 kJ mol^{-1} when δ in the range of 0.05–0.40. The following thermodynamic analysis will be based on these results for discussion.

$$\Delta H_{red}^{\ominus}(\delta) = 58.529 + 71.905\delta + 905.361\delta^2 - 1724.966\delta^3 \quad (17)$$

3.2. Solar-to-fuel efficiency analysis for LCZ-73 based solar CO production system

3.2.1. Decreasing P_{O_2} *via* vacuum pump. In the case of decreasing the oxygen partial pressure by vacuum pump, then no sweep gas is needed and $Q_{Ar\ heating} = 0$. Solar-to-fuel efficiency of the two-step solar thermochemical CO_2 splitting based on LCZ-73 perovskite as functions of reduction temperature and
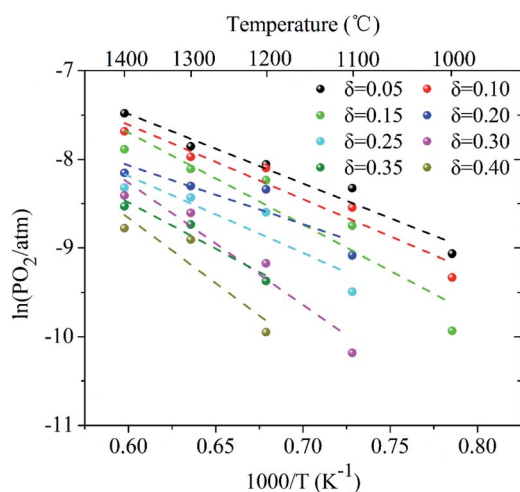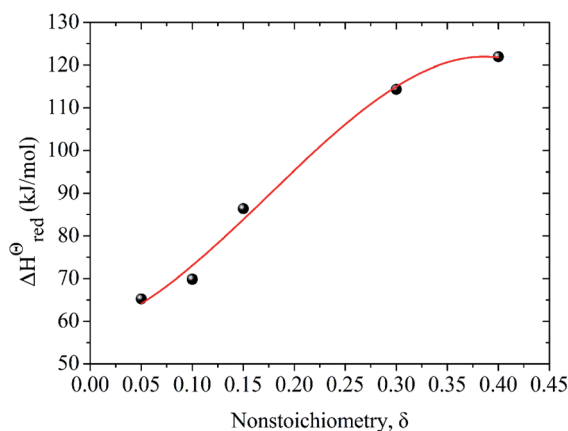
Fig. 4 Variation of reduction enthalpy of $LaCo_{0.7}Zr_{0.3}O_3$ (LCZ-73) as a function of oxygen non-stoichiometry δ.

the ratio of n_{CO_2}/n_{LCZ-73} with different heat exchange coefficients $\varepsilon_{heat\ exchanger}$ is analyzed in the range of reduction temperature of 1000–1400 °C and oxidation at 800 °C and is shown in Fig. 5(a)–(d). Meanwhile, the relationship between the ratio of n_{CO_2}/n_{LCZ-73} corresponding to $\eta_{solar-to-fuel} = 20\%$ and reduction temperatures is shown in Fig. 5(e).

As shown in Fig. 5(a)–(d), at the molar ratio of $n_{CO_2}/n_{LCZ-73} \leq 500$, $\eta_{solar-to-fuel}$ decreases rapidly with the increase of the ratio, and decreases slowly when the molar ratio is greater than 500. In Fig. 5(a)–(c), $\eta_{solar-to-fuel} \leq 1\%$ at $n_{CO_2}/n_{LCZ-73} \geq 500$, the molar ratio of n_{CO_2}/n_{LCZ-73} is enlarged to 1000 in Fig. 5(d). This also means that higher efficiency can be achieved with higher heat recovery. This can also be found from Fig. 5(a)–(d) that with the increase of $\varepsilon_{heat\ exchanger}$, $\eta_{solar-to-fuel}$ increases gradually. In the current experimental situation, the molar ratio of n_{CO_2}/n_{LCZ-73} is $2737 : 1$, $\eta_{solar-to-fuel} = 0.39\%$ is obtained at the reduction temperature of 1300 °C with 75% heat recovery. While, when no heat recovery is considered, this efficiency is just 0.1%.

The insets are the partial enlargements with the molar ratio of less than 50. Overall, under the same conditions, the highest $\eta_{solar-to-fuel}$ is achieved at 1300 °C and $n_{CO_2}/n_{LCZ-73} \geq 5$ in Fig. 5(a)–(c) and $n_{CO_2}/n_{LCZ-73} \geq 10$ in Fig. 5(d). When the ratio of $n_{CO_2}/n_{LCZ-73} < 10$, $\eta_{solar-to-fuel}$ will reach 20% or more in Fig. 5(a)–(c) and for higher heat recovery in Fig. 5(d), $\eta_{solar-to-fuel}$ of 20% can be achieved at $n_{CO_2}/n_{LCZ-73} < 50$. This efficiency value is also proposed based on estimated qualitatively in reference and is considered as the benchmark for commercially achievable system-level annual average solar-to-fuel efficiency for a viable alternative to conventional electrolysis.[44] For this competitive efficiency reference value, further analysis is shown in Fig. 5(e). When the efficiency reaches 20%, $n_{CO_2}/n_{LCZ-73} = 47.59$ at 1300 °C, and $n_{CO_2}/n_{LCZ-73} = 35.12$ at 1000 °C with 75% heat recovery. The molar ratios of n_{CO_2}/n_{LCZ-73} are 12.4 and 6.74 with no heat recovery, respectively. Compared with higher temperature conditions (1300 and 1400 °C), the molar ratio of n_{CO_2}/n_{LCZ-73} at low temperature requires more demanding conditions with the prospects of commercialization. This is still a big challenge in the current research background of thermochemical fuels. However, under the same conditions, the larger molar ratio of n_{CO_2}/n_{LCZ-73} is more accessible under current technical conditions.
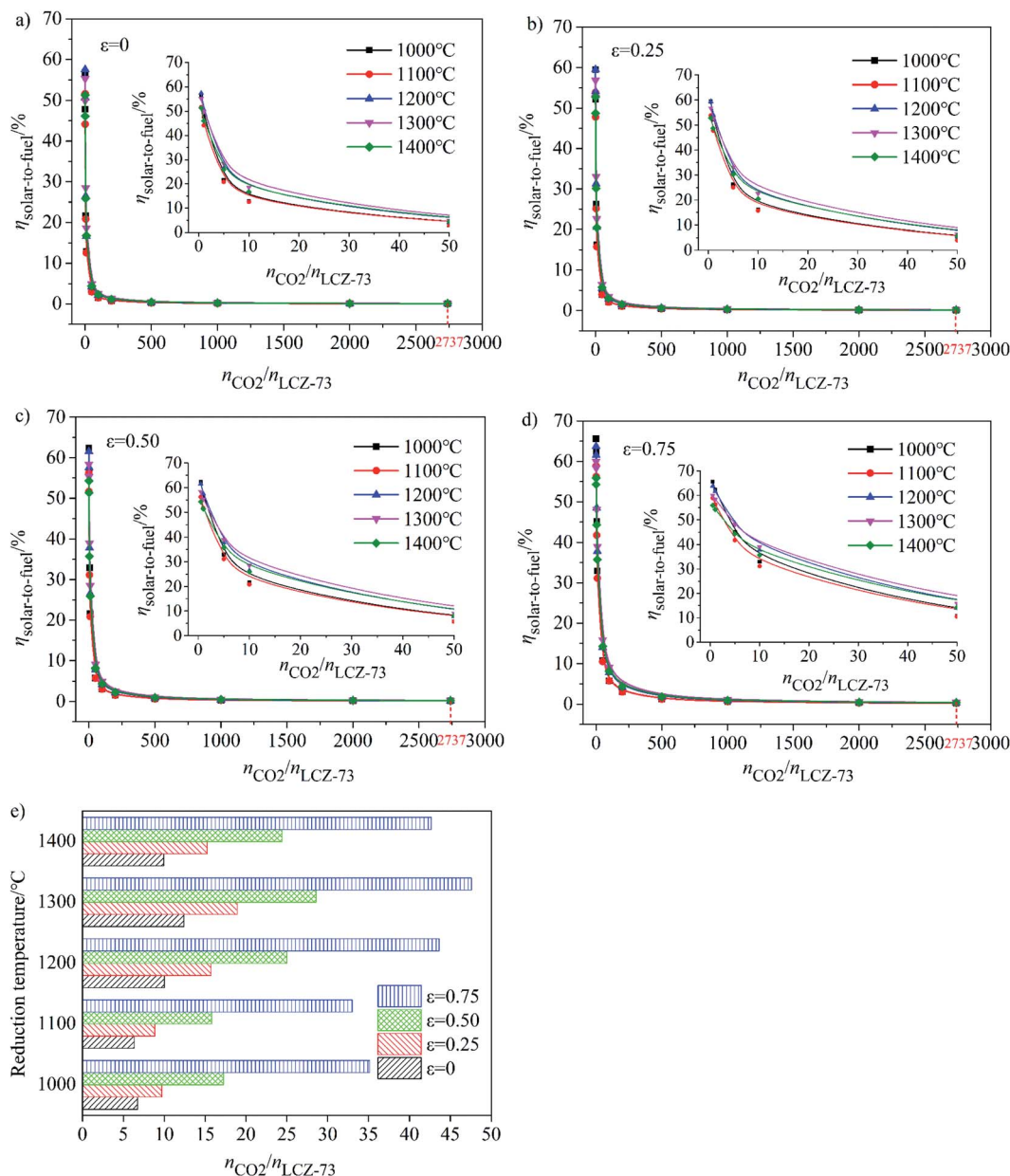
Fig. 3 Arrhenius plots of oxygen partial pressure *versus* inverse temperature for $LaCo_{0.7}Zr_{0.3}O_3$ (LCZ-73) corresponding to fixed δ between 0.05 and 0.40.

Fig. 5 Solar-to-fuel efficiency ($\eta_{\text{solar-to-fuel}}$) as functions of reduction temperature and molar ratio of CO_2 to perovskite and the molar ratio of reactants required to achieve $\eta_{\text{solar-to-fuel}} = 20\%$ under different heat recovery conditions when using a vacuum pump to reduce oxygen partial pressure. (a)–(d) $\eta_{\text{solar-to-fuel}}$ as functions of reduction temperature and molar ratio of CO_2 to LCZ-73 under different heat exchange coefficients $\varepsilon_{\text{heat exchanger}}$. (e) Molar ratio of CO_2 to perovskite corresponding to $\eta_{\text{solar-to-fuel}} = 20\%$ with the reduction at 1000–1400 °C and oxidation at 800 °C.

3.2.2. Decreasing P_{O_2} via vacuum pump combined with Ar sweeping. When inert gas purging is used to reduce oxygen partial pressure, then no vacuum pump is needed and $Q_{\text{pump}} = 0$. A strategy of combined vacuum pump with Ar purging during the reduction process was adopted to reduce the partial pressure of oxygen in the reaction chamber rapidly and reduce the amount of Ar required for purging. It has also been shown that the combination of reducing the oxygen partial pressure via vacuum pump and inert sweeping helps to increase the efficiency of the inert-swept reactor.[31] The evolution of $\eta_{\text{solar-to-fuel}}$ as functions of reduction temperature and molar ratio of CO_2 to

LCZ-73 with different heat exchange coefficients $\varepsilon_{\text{heat exchanger}}$ is depicted in Fig. 6(a)–(d). As shown, in the reduction temperature range of 1000–1400 °C, $\eta_{\text{solar-to-fuel}}$ decreases rapidly as the molar ratio of CO_2 to perovskite increases. When $n_{CO_2}/n_{\text{LCZ-73}} \geq 1000$, $\eta_{\text{solar-to-fuel}} < 1\%$, regardless of the temperature is in this range, especially in Fig. 6(a)–(c), the range of this ratio expanded to $n_{CO_2}/n_{\text{LCZ-73}} \geq 500$. In Fig. 6(d), $\varepsilon_{\text{heat exchanger}} = 0.75$, $\eta_{\text{solar-to-fuel}} > 1\%$ at $n_{CO_2}/n_{\text{LCZ-73}} \leq 500$. When $n_{CO_2}/n_{\text{LCZ-73}} < 500$, the efficiency slowly increases as the ratio decreases. For $n_{CO_2}/n_{\text{LCZ-73}} < 200$, the efficiency increases rapidly as the ratio decreases. When it comes to the ratio of $n_{CO_2}/n_{\text{LCZ-73}} \leq 200$, $\eta_{\text{solar-to-fuel}} >$

1% except in the case of $\varepsilon_{\text{heat exchanger}} = 0$ and reduction temperatures of 1000–1100 °C. With the increase of $\varepsilon_{\text{heat exchanger}}$, $\eta_{\text{solar-to-fuel}}$ at different temperatures are improved and reached the highest at 1300 °C. Under the experimental conditions of this work, the flow rate of CO_2 is 40 sccm, the molar ratio of $n_{CO_2}/n_{\text{LCZ-73}} = 2737$, $\eta_{\text{solar-to-fuel}} = 0.1\%$ without considering heat recovery at the reduction temperature of 1300 °C, $\eta_{\text{solar-to-fuel}} = 0.39\%$ with 75% heat recovery. For a theoretical deduction, if the molar ratio of $n_{CO_2}/n_{\text{LCZ-73}}$ can be further reduced to 0.5, the theoretical maximum value of $\eta_{\text{solar-to-fuel}}$ of 52.5% and 59.6% can be achieved with no heat recovery

and 75% heat recovery were considered, respectively. Despite this considerable efficiency value, it is necessary to know that such a low ratio poses great challenges for experimental verification. The inset in each figure of Fig. 6(a)–(d) is for partial amplification in the range of molar ratio less than 50. It can be seen from the insets that the highest efficiency value is obtained over the entire molar ratio when the reduction temperature is 1300 °C, and the lowest value at 1000 °C. At this point we consider a considerable solar-to-fuel efficiency value of 20% which is a viable alternative with that more traditional and reliable technology based on electrolysis.[44]
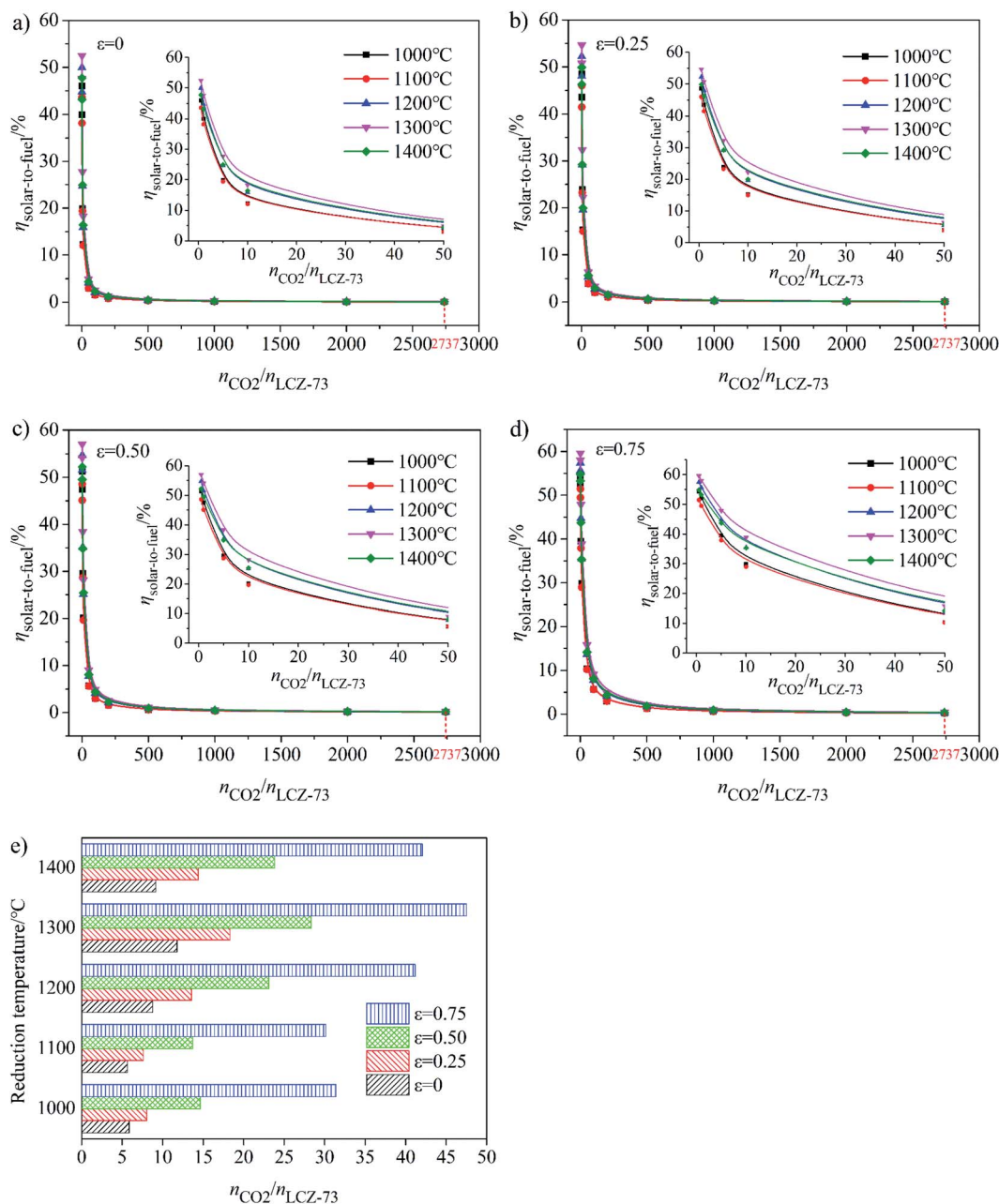
Fig. 6 Solar-to-fuel efficiency ($\eta_{\text{solar-to-fuel}}$) as functions of reduction temperature and molar ratio of CO_2 to perovskite and the molar ratio of reactants required to achieve $\eta_{\text{solar-to-fuel}} = 20\%$ under different heat recovery conditions when using vacuum pump combined with gas purging to reduce oxygen partial pressure. (a)–(d) $\eta_{\text{solar-to-fuel}}$ as functions of heat exchange coefficient $\varepsilon_{\text{heat exchanger}}$ and molar ratio of CO_2 to LCZ-73. (e) Variation of molar ratio of CO_2 to LCZ-73 corresponding to $\eta_{\text{solar-to-fuel}} = 20\%$ with the reduction at 1000–1400 °C and oxidation at 800 °C.

Variation of molar ratio of n_{CO_2}/n_{LCZ-73} corresponding to the solar-to-fuel efficiency of 20% with heat exchange coefficient $\varepsilon_{heat\ exchanger}$ at different reduction temperatures was shown in Fig. 6(e). Similarly, we find that when the efficiency reaches 20% and as the benchmark, the ratio of n_{CO_2}/n_{LCZ-73} is maximum at 1300 °C, reaching about 50, which is the easiest to reach in the temperature range in question. At the same time, this means that if there is a more efficient way to reduce the ratio of n_{CO_2}/n_{LCZ-73}, then at 1300 °C, solar-to-fuel efficiency will be higher than 20%. This is a great encouragement for commercialization. However, in most of the current experimental studies of two-step solar thermochemical fuel production cycles, the far excessive amount of oxidant in oxidation step is used for a high fuel production. How to effectively reduce the amount of oxidant introduced into the oxidation step becomes the key to improve the solar-to-fuel efficiency. Another finding is that as the heat exchange coefficient increases, n_{CO_2}/n_{LCZ-73} at the same temperature changes monotonously, indicating that as the heat recovery increases, the conditions for commercialization are more moderate, and the solar-to-fuel efficiency is higher.

3.2.3. Analysis of the energy for CO_2 heating.
Fig. 7 shows the relationship between the energy of each part and reduction temperature during the solar two-step thermochemical CO_2 splitting process via Ar purging. The variations of energy with reduction temperature and the relative magnitude are shown in Fig. 7(a). It can be seen that Q_{red}, Q_{LCZ-73}, Q_{oxi}, Q_{rec} and the fuel energy generated increase with the increase of reduction temperature. The energy required for the reduction reaction is the minimum, while the energy required for the sample heating and the oxidation reaction is the maximum of the energy consumption items mentioned above. The energy required for heating Ar as functions of reduction temperature and heat exchange coefficient of heat exchanger is shown in Fig. 7(b). We can find that the energy consumed for heating Ar increases with the increase of reduction temperature, and this value at 1400 °C is about twice of that at 1000 °C. At the same temperature, the energy consumed decreases with the increase of heat exchange coefficient $\varepsilon_{heat\ exchanger}$.

Similarly, the energy consumed for CO_2 heating with heat recovery as functions of reduction temperature and molar ratio of n_{CO_2}/n_{LCZ-73} is given in Fig. 8(a). The molar ratio of n_{CO_2}/n_{LCZ-73} increases as the amount of CO_2 increases, and the energy consumed for CO_2 heating increases significantly. When n_{CO_2}/n_{LCZ-73} varies from 100 to 1000, the energy consumed increases by a corresponding multiple. Compared with the molar ratio of n_{CO_2}/n_{LCZ-73}, the reduction temperature has much smaller impact on the energy consumed for CO_2 heating. The energy increases slightly with the increase of reduction temperature, but the trend is gentle. The energy for CO_2 heating is two or three orders of magnitude higher than those in Fig. 7(a) and (b).

Finally, the proportion of energy required for CO_2 heating in total input energy is summarized in Fig. 8(b). It can be seen that the proportion rapidly increases with the increase of n_{CO_2}/n_{LCZ-73}, but decreases slightly with the increase of the reduction temperature, which is mainly because the reduction temperature has little influence on the energy of CO_2 heating, but has great impact on the total input energy. With the increase of heat exchanger coefficient, the proportion of energy consumption for CO_2 heating gradually decreases. As the molar ratio of n_{CO_2}/n_{LCZ-73} increases, the proportion of energy for CO_2 heating in total input energy increases rapidly, resulting in lower solar-to-fuel efficiency. At 1300 °C and $\varepsilon_{heat\ exchanger} = 0.5$, when $n_{CO_2}/n_{LCZ-73} = 0.5$, the proportion of CO_2 heating is only 5.35%, while, when $n_{CO_2}/n_{LCZ-73} = 50$, the proportion reaches nearly 85.0%. When the amount of CO_2 is further increased, this proportion reaches 95.8% as the ratio of n_{CO_2}/n_{LCZ-73} increased to 200. This also reveals the reason why the current thermochemical fuel research is less efficient.

3.2.4. The effect of CO_2 flow rates on solar-to-fuel efficiency.
In order to explore the thermodynamic properties of perovskite LCZ-73 based thermochemical CO_2 splitting under different CO_2 content atmospheres, experimental tests are carried out with different CO_2 content in Ar. Approximately 10 mg LCZ-73 powder is used for each test and the sample is heated to 1300 °C in Ar (80 sccm) with the ramp of 10 °C min^{-1} and maintained for 60 min. Then the sample is cooled down to 800 °C for oxidation with the ramp of 20 °C min^{-1} and
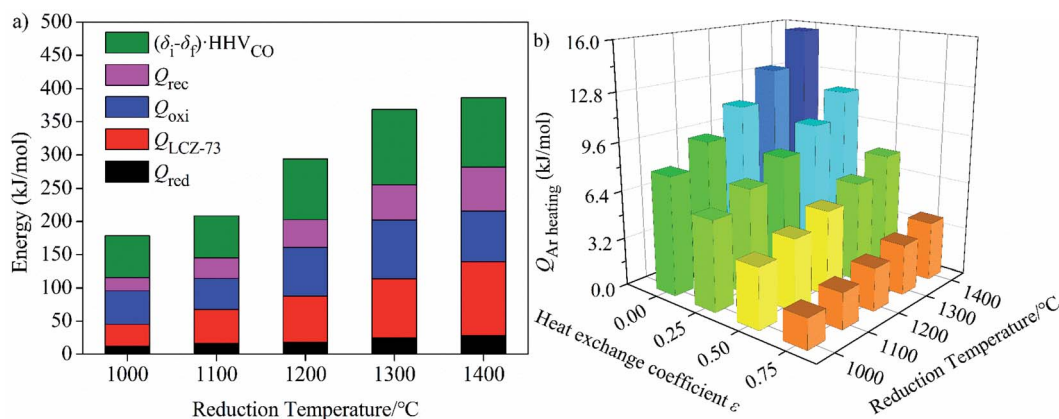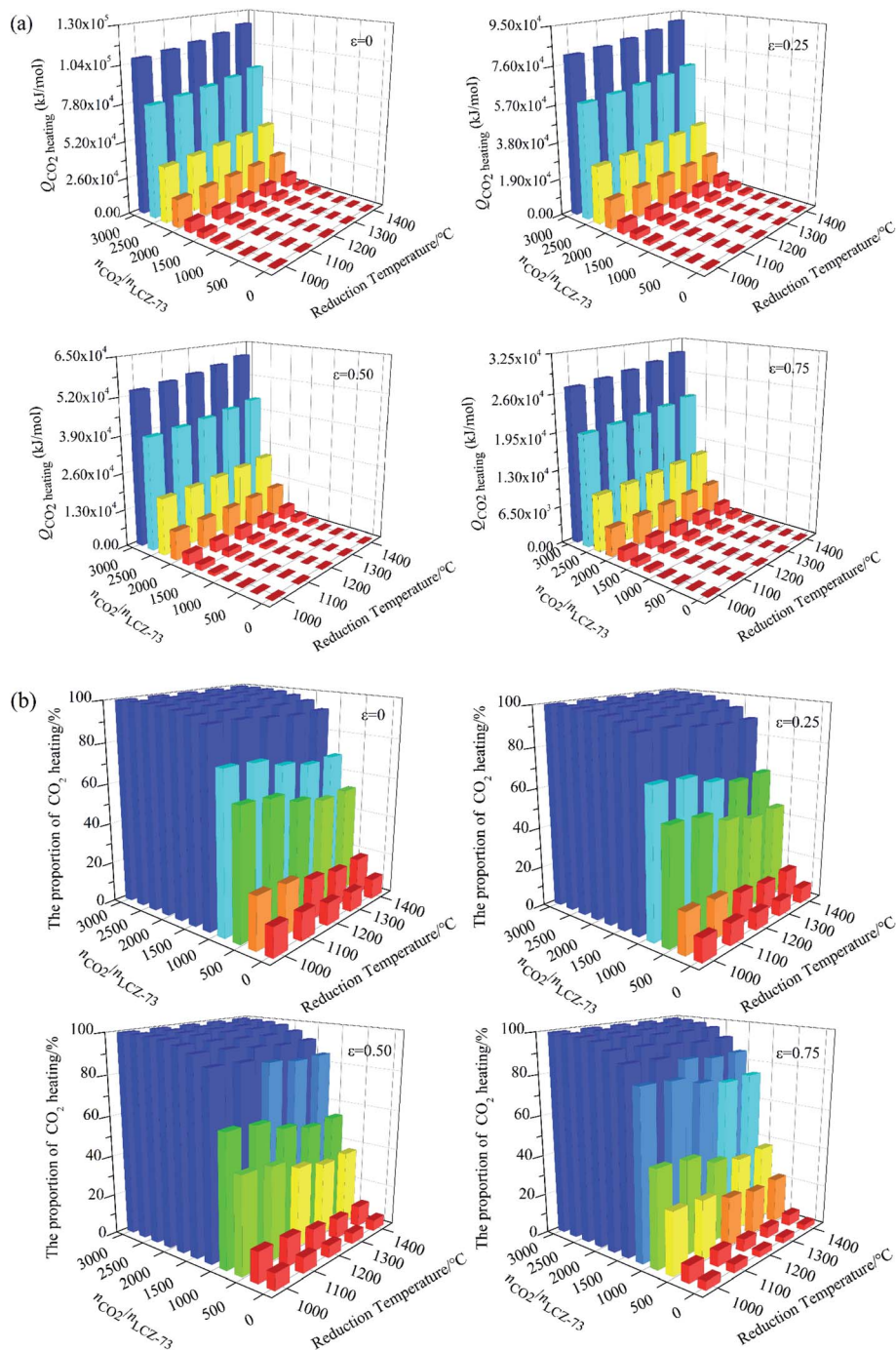

Fig. 7 Relationship between the energy and reduction temperature during the solar two-step thermochemical CO_2 splitting process via Ar purging. (a) Energy required as a function of reduction temperature, (b) energy required for Ar heating as functions of reduction temperature and heat transfer coefficient $\varepsilon_{heat\ exchanger}$.

Fig. 8 Energy for CO_2 heating as functions of reduction temperature and molar ratio of n_{CO_2}/n_{LCZ-73} under different heat recovery conditions. (a) Energy required for CO_2 heating and (b) the proportion of energy for CO_2 heating in total input energy as functions of reduction temperature and molar ratio of n_{CO_2}/n_{LCZ-73} with different heat transfer coefficients $\varepsilon_{heat\ exchanger}$.

maintained for 60 min in the atmosphere of 10–70 sccm CO_2 balanced with Ar, the corresponding ratio of n_{CO_2}/n_{LCZ-73} varies from 684 to 4788, the total gas flow is maintained at 80 sccm. The CO yield and solar-to-fuel efficiency as functions of CO_2 flow rate are obtained and calculated based on the thermodynamic model mentioned above. The details are shown in Fig. 9.

As shown, the effects of CO_2 flow rate on CO yield and solar-to-fuel efficiency at various heat exchanger coefficient $\varepsilon_{heat\ exchanger}$ are analyzed. It can be clearly seen from Fig. 9(a) that

the yield of CO increases gradually with the increase of CO_2 flow rate, and the high CO_2 concentration is favorable for the oxidation reaction. At the same time, the ratio of n_{CO_2}/n_{CO} changes monotonically with the increase of CO_2 flow rate. When the CO_2 flow rate in the oxidation step is 10 sccm, $n_{CO_2}/n_{LCZ-73} = 684$, $n_{CO_2}/n_{CO} = 1926$, and the same value is 10 648 when the CO_2 flow rate is 70 sccm at $n_{CO_2}/n_{LCZ-73} = 4788$, the latter represents an increase of nearly 27% in CO yield over the former. However, it is also noted that solar-to-fuel efficiency is
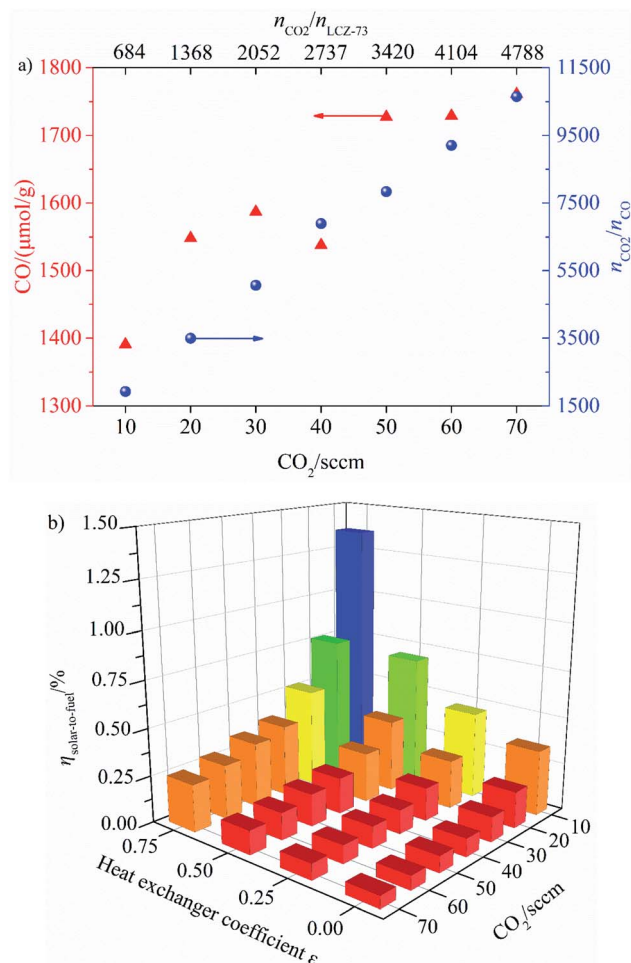
Fig. 9 CO yield and solar-to-fuel efficiency as functions of CO_2 flow rate.

pump and vacuum pump combined with inert gas purge to reduce oxygen partial pressure and CO_2 heating on the performance parameter $\eta_{\text{solar-to-fuel}}$ have been analyzed with the consideration of gas–gas, gas–solid phase heat recuperation. The energy cost of CO_2 heating during the redox process is underscored. At the oxygen partial pressure of 10^{-5} bar, non-stoichiometric oxygen δ increases by more than 3 times as the reduction temperature increases from 1000 °C to 1300 °C. However, the deviation of δ is negligible between 1300 °C and 1400 °C. The reaction enthalpy ranges from 60 to 130 kJ mol^{-1} corresponding to δ = 0.05–0.40. Comparing $\eta_{\text{solar-to-fuel}}$ *via* vacuum pump with the case of vacuum pump combined with inert gas purging, the efficiencies of 0.39% and 0.1% can be achieved with 75% and without heat recovery under experimental conditions, respectively. Based on the energy analysis, the energy cost of CO_2 heating took up the bulk of energy consumption of the thermodynamic process as the $n_{CO_2}/n_{\text{LCZ-73}}$ increases, which is two or three orders of magnitude higher than other heating items. Compared with higher temperature conditions, $n_{CO_2}/n_{\text{LCZ-73}}$ at lower temperature requires more demanding conditions for the aim of commercialization. Finally, the ability of the perovskite LCZ-73 to split CO_2 and thermochemical performance were tested under different CO_2 flow rates. The results show that high CO_2 flow rate is conductive to the production of CO, but at the cost of low $\eta_{\text{solar-to-fuel}}$. The maximum solar-to-fuel efficiencies of 1.36% and 0.35% are achieved with 75% heat recovery and without heat recovery with the CO_2 flow rate of 10 sccm. However, values under the same heat exchange conditions are only 0.25% and 0.06% with the CO_2 flow rate of 70 sccm. On the premise of meeting the requirements of the experimental device, further experiments are needed to verify the ability of the perovskite to split CO_2 at lower CO_2 flow rate (*e.g.*, less than 10 sccm, $n_{CO_2}/n_{\text{LCZ-73}}$ < 684).

negatively correlated with the increase of CO_2 flow rate in Fig. 9(b). Although CO yield is low at low CO_2 flow rate, solar-to-fuel efficiency is high. In order to prove that this material can still split CO_2 under the condition of lower molar ratios, further experiments would be needed for verification, such as the CO_2 flow rate is less than 10 sccm ($n_{CO_2}/n_{\text{LCZ-73}}$ < 684). It should be noted that an excessively low CO_2 flow rate may impose higher requirements on the experimental devices in actual operation. Considering the effect of heat transfer coefficient, solar-to-fuel efficiency increases with the increase of heat transfer coefficient at the same CO_2 flow rate. The maximum solar-to-fuel efficiencies of 1.36% and 0.35% are achieved with 75% heat recovery and without heat recovery with the CO_2 flow rate of 10 sccm ($n_{CO_2}/n_{\text{LCZ-73}}$ = 684). However, the solar-to-fuel efficiencies under the same heat exchange conditions are only 0.25% and 0.06% with the CO_2 flow rate of 70 sccm.

4. Conclusions

This work performs the performance evaluation towards the doped perovskite LaCo$_{0.7}$Zr$_{0.3}$O$_3$ (LCZ-73) based thermochemical CO_2 splitting process thermodynamically *via* the experimentally derived parameters for the first time. The impacts of vacuum

Nomenclature

M	The molar mass of perovskite, g mol^{-1}
m	Mass of the matter, g
$\bar{R}$	Universal molar gas constant, 8.314 J mol^{-1} K^{-1}
T	Temperature, K
K	The equilibrium constant
P	Pressure, atm
Q	The energy required or recovered for each process, J mol^{-1}
$\bar{C}_p$	The specific molar heat capacity, J mol^{-1} K^{-1}
n	Amount of substance, mol
HHV	Higher heating value, J mol^{-1}
C	Solar concentration ratio, suns
I	1000 W m^{-2}
$n_{CO_2}/n_{\text{LCZ-73}}$	Molar ratio of CO_2 to perovskite LaCo$_{0.7}$Zr$_{0.3}$O$_3$

Greek symbols

Δm	Mass change, g

δ	Nonstoichiometric oxygen
$\Delta G^{\ominus}$	Standard molar Gibbs free energy, J mol^{-1}
$\Delta H_{red}^{\ominus}$	Standard molar enthalpy for reduction, J mol^{-1}
$\Delta S_{red}^{\ominus}$	Standard molar entropy for reduction, J mol^{-1}
$\Delta\delta$	Non-stoichiometry change
ΔQ	The energy change in a process, J mol^{-1}
ΔT	Temperature swing, K
$\eta_{S\to W}$	Solar energy to vacuum pumping conversion efficiency
$\varepsilon_{heat\ exchanger}$	The heat exchange coefficient of the heat exchanger
ε_{rec}	The effectiveness of heat recovery, 0.6
η_{abs}	Heat absorption efficiency of solar reactor
σ	Stefan–Boltzmann constant, 5.67×10^{-8} W m^{-2} K^{-4}
$\eta_{solar-tio-fuel}$	Solar to fuel conversion efficiency

Subscripts

O	Oxygen atom
O_2	Oxygen gas
red	Reduction
oxi	Oxidation
i	The state of non-stoichiometric oxygen after reduction
f	The state of non-stoichiometric oxygen after oxidation
pump	Vacuum pump
0	The atmospheric pressure, 1 atm
Ar heating	Preheat the sweeping gas Ar
amb	Ambient condition
CO_2	Carbon dioxide
CO	Carbon monoxide
rec	Recovery
CO_2 heating	Preheat the CO_2 gas
abs	Absorption

Superscripts

Θ	Standard condition at T and P_{atm}

Abbreviations

LCZ-73	$LaCo_{0.7}Zr_{0.3}O_3$

Conflicts of interest

There are no conflicts to declare.

References

1 A. M. A. Hussein, K. G. Burra, G. Bassioni, R. M. Hammouda and A. K. Gupta, *Appl. Energy*, 2019, **235**, 1183–1191.

2 R. R. Bhosale, A. Kumar, F. AlMomani, U. Ghosh, D. Dardor, Z. Bouabidi, M. Ali, S. Yousefi, A. AlNouss, M. S. Anis, M. H. Usmani, M. H. Ali, R. S. Azzam and A. Banu, *Energy Convers. Manage.*, 2016, **112**, 413–422.

3 Y. W. Zhao, Y. D. Zhang, W. J. Li, Y. Hao and H. G. Jin, *J. Cleaner Prod.*, 2018, **176**, 758–769.

4 S. Chuayboon and S. Abanades, *J. Cleaner Prod.*, 2019, **232**, 784–795.

5 J. Huang, Y. Fu, S. Li, W. Kong, J. Zhang and Y. Sun, *J. CO2 Util.*, 2018, **27**, 450–458.

6 F. A. Costa Oliveira, M. A. Barreiros, S. Abanades, A. P. F. Caetano, R. M. Novais and R. C. Pullar, *J. CO2 Util.*, 2018, **26**, 552–563.

7 S. Chuayboon, S. Abanades and S. Rodat, *J. Energy Chem.*, 2020, **41**, 60–72.

8 M. Takacs, M. Hoes, M. Caduff, T. Cooper, J. R. Scheffe and A. Steinfeld, *Acta Mater.*, 2016, **103**, 700–710.

9 A. H. Bork, E. Povoden-Karadeniz and J. L. M. Rupp, *Adv. Energy Mater.*, 2017, **7**, 1601086.

10 S. Dey, B. S. Naidu and C. N. Rao, *Chemistry*, 2015, **21**, 7077–7081.

11 S. Dey, B. S. Naidu, A. Govindaraj and C. N. Rao, *Phys. Chem. Chem. Phys.*, 2015, **17**, 122–125.

12 M. M. Nair and S. Abanades, *Sustainable Energy Fuels*, 2018, **2**, 843–854.

13 S. Mulmi, H. M. Chen, A. Hassan, J. F. Marco, F. J. Berry, F. Sharif, P. R. Slater, E. P. L. Roberts, S. Adams and V. Thangadurai, *J. Mater. Chem. A*, 2017, **5**, 6874–6883.

14 S. Dey, B. S. Naidu and C. N. Rao, *Dalton Trans.*, 2016, **45**, 2430–2435.

15 C. L. Muhich, S. Blaser, M. C. Hoes and A. Steinfeld, *Int. J. Hydrogen Energy*, 2018, **43**, 18814–18831.

16 M. Ezbiri, M. Takacs, B. Stolz, J. Lungthok, A. Steinfeld and R. Michalsky, *J. Mater. Chem. A*, 2017, **5**, 15105–15115.

17 M. E. Galvez, R. Jacot, J. Scheffe, T. Cooper, G. Patzke and A. Steinfeld, *Phys. Chem. Chem. Phys.*, 2015, **17**, 6629–6634.

18 A. Demont and S. Abanades, *J. Mater. Chem. A*, 2015, **3**, 3536–3546.

19 T. Cooper, J. R. Scheffe, M. E. Galvez, R. Jacot, G. Patzke and A. Steinfeld, *Energy Technol.*, 2015, **3**, 1130–1142.

20 A. H. Bork, M. Kubicek, M. Struzik and J. L. M. Rupp, *J. Mater. Chem. A*, 2015, **3**, 15546–15557.

21 A. Demont and S. Abanades, *RSC Adv.*, 2014, **4**, 54885–54891.

22 G. Takalkar and R. R. Bhosale, *Fuel*, 2019, **254**, 115624.

23 Q. Jiang, J. Tong, G. Zhou, Z. Jiang, Z. Li and C. Li, *Sol. Energy*, 2014, **103**, 425–437.

24 J. P. Säck, S. Breuer, P. Cotelli, A. Houaijia, M. Lange, M. Wullenkord, C. Spenke, M. Roeb and C. Sattler, *Sol. Energy*, 2016, **135**, 232–241.

25 C. N. R. Rao and S. Dey, *Proc. Natl. Acad. Sci. U. S. A.*, 2017, **114**, 13385–13393.

26 R. J. Carrillo and J. R. Scheffe, *Energy Fuels*, 2019, **33**, 12871–12884.

27 A. H. Bork, E. Povoden-Karadeniz, A. J. Carrillo and J. L. M. Rupp, *Acta Mater.*, 2019, **178**, 163–172.

28 L. Wang, T. Ma, S. Dai, T. Ren, Z. Chang, L. Dou, M. Fu and X. Li, *Chem. Eng. J.*, 2020, **389**, 124426.

29 J. Vieten, B. Bulfin, M. Senholdt, M. Roeb, C. Sattler and M. Schmücker, *Solid State Ionics*, 2017, **308**, 149–155.

30 Y. Hao, C.-K. Yang and S. M. Haile, *Chem. Mater.*, 2014, **26**, 6073–6082.

31 I. Ermanoski, N. P. Siegel and E. B. Stechel, *J. Sol. Energy Eng.*, 2013, **135**, 10.

32 H. Kong, Y. Hao and H. Jin, *Appl. Energy*, 2018, **228**, 301–308.

33 B. Bulfin, F. Call, M. Lange, O. Lübben, C. Sattler, R. Pitz-Paal and I. V. Shvets, *Energy Fuels*, 2015, **29**, 1001–1009.

34 B. J. McBride, S. Gordon and M. A. Reno, *NASA Tech. Pap. 3287*, 1993, p. 16.

35 J. E. Miller, M. D. Allendorf, R. B. Diver, L. R. Evans, N. P. Siegel and J. N. Stuecker, *J. Mater. Sci.*, 2008, **43**, 4714–4728.

36 H. Wang, M. Liu, H. Kong and Y. Hao, *Appl. Therm. Eng.*, 2018, **152**, 925–936.

37 R. R. Bhosale, A. Kumar and P. Sutar, *Energy Convers. Manage.*, 2017, **135**, 226–235.

38 S. Li, V. M. Wheeler, P. B. Kreider, R. Bader and W. Lipiński, *Energy Fuels*, 2018, **32**, 10848–10863.

39 B. D. Ehrhart, C. L. Muhich, I. Al-Shankiti and A. W. Weimer, *Int. J. Hydrogen Energy*, 2016, **41**, 19881–19893.

40 S. Abanades, P. Charvin, G. Flamant and P. Neveu, *Energy*, 2006, **31**, 2805–2822.

41 L. Wang, T. Ma, Z. Chang, H. Li, M. Fu and X. Li, *Sol. Energy*, 2019, **177**, 772–781.

42 Y. Hao, J. Jin and H. Jin, *Appl. Therm. Eng.*, 2019, **166**, 113600.

43 R. J. Panlener, R. N. Blumenthal and J. E. Garnier, *J. Phys. Chem. Solids*, 1975, **36**, 1213–1222.

44 N. P. Siegel, J. E. Miller, I. Ermanoski, R. B. Diver and E. B. Stechel, *Ind. Eng. Chem. Res.*, 2013, **52**, 3276–3286.